## Title

A Cohesive-Zone-Based Contact Mechanics Analysis of Delamination in Homogeneous and Layered Half-Spaces Subjected to Normal and Shear Surface Tractions



## Journal

Journal of Applied Mechanics, 90(7)

## ISSN

0021-8936

## Authors

Cen, Jialiang
Komvopoulos, Kyriakos

## Publication Date

2023-07-01

## DOI

10.1115/1.4062141

Peer reviewed

# A Cohesive-Zone-Based Contact Mechanics Analysis of Delamination in Homogeneous and Layered Half-Spaces Subjected to Normal and Shear Surface Tractions

**Jialiang Cen**
Department of Mechanical Engineering,
University of California,
Berkeley, CA 94720
e-mail: artoscen@berkeley.edu

**Kyriakos Komvopoulos**[1]
Professor
Department of Mechanical Engineering,
University of California,
Berkeley, CA 94720
e-mail: kyriakos@me.berkeley.edu

*A contact mechanics analysis of interfacial delamination in elastic and elastic-plastic homogeneous and layered half-spaces due to normal and shear surface tractions induced by indentation and sliding was performed using the finite element method. Surface separation at the delamination interface was controlled by a surface-based cohesive zone constitutive law. The instigation of interfacial delamination was determined by the critical separation distance of interface node pairs in mixed-mode loading based on a damage initiation criterion exemplified by a quadratic relation of the interfacial normal and shear tractions. Stiffness degradation was characterized by a linear relation of the interface cohesive strength and a scalar degradation parameter, which depended on the effective separation distances corresponding to the critical effective cohesive strength and the fully degraded stiffness, defined by a mixed-mode loading critical fracture energy criterion. Numerical solutions of the delamination profiles, the subsurface stress field, and the development of plasticity illuminated the effects of indentation depth and sliding distance on interfacial delamination in half-spaces with different elastic-plastic properties, interfacial cohesive strength, and layer thickness. Simulations yielded insight into the layer and substrate material property mismatch on interfacial delamination. A notable contribution of the present study is the establishment of a computational mechanics methodology for developing plasticity-induced cumulative damage models for multilayered structures.*
[DOI: 10.1115/1.4062141]

*Keywords: cohesive strength, computational mechanics, damage, delamination, plasticity, stress analysis*

## 1 Introduction

Delamination is commonly observed in multilayered structures used in various applications, such as semiconductor devices [1], electronics packaging [2], plastic packaging [3], high-performance capacitors [4], sliding wear [5,6], cutting tools [7,8], thermal barrier coatings for turbines [9] and automotive engines [10], and high-temperature materials [11]. This phenomenon is controlled by an interfacial cohesive strength toughness parameter which, together with the mechanical properties of the layer and substrate materials, controls the inception of failure. Low interfacial cohesive strength can lead to layer delamination, thereby not serving the desired purpose of preserving the integrity of the substrate and close-fitting design tolerances. A layered structure may also evolve from an initially uniform structure during fabrication and/or usage. A characteristic example is the development of a strain-hardened surface layer on a machined part or a load bearing component. Therefore, even an initially homogeneous structure can ultimately become a layered structure during fabrication and/or usage. Consequently, basic understanding of interfacial delamination prompted by the mismatch of the layer and substrate physical properties is critical to the reliability and functionality of structures subjected to thermomechanical loadings.

Various experimental and computational methods have been used to study interfacial delamination in layered structures. Gerberich et al. [12] identified five sequential stages of plasticity and interface fracture due to nanoindentation resulting in layer decohesion from the substrate (delamination). It was reported that activation of dislocations followed by hardening and material pile-up around the nanoindenter were the precursors of plasticity-induced delamination at the layer/substrate interface. He et al. [13] designed a test method for measuring the delamination toughness of bilayer coatings attached to non-planar components, which was guided by beam-theory solutions of the energy release rate and the structure compliance. In addition, they used the finite element method (FEM) to study the effect of residual stress on the energy release rate and determined that the shear-to-normal stress ratio was highly dependent on the layer thickness and the modulus ratio of the two layers comprising the bilayer coating. Liu and Yang [14] performed an FEM analysis of interfacial delamination in an indented stiff layer/compliant substrate system and obtained numerical results showing that both the delamination zone and the maximum nodal separation increased with the indentation depth and the decrease of the layer thickness.

Significant advancements in fundamental understanding of interfacial delamination have been achieved by implementing cohesive constitutive laws in FEM analysis. The concept of a cohesive zone model (CZM), proposed by Dugdale [15] and Barenblatt

[1]Corresponding author.

Contributed by the Applied Mechanics Division of ASME for publication in the Journal of Applied Mechanics. Manuscript received January 30, 2023; final manuscript received March 11, 2023; published online April 6, 2023. Assoc. Editor: Jian Wu.

  

[16], has been widely used to analyze localized damage or plastic flow in the close proximity of crack tips. Subsequently, various cohesive zone laws (in the form of interface traction-separation relationships accounting for elastic and softening deformation prior to final failure) were integrated in the analyses of crack initiation and growth and interfacial fracture. Alfano et al. [17] performed a comparative study of various CZMs used to model the instigation of interfacial cracking and delamination.

The integration of CZMs in FEM studies provided an effective computational methodology for undertaking complex interface problems in layered structures. For instance, Yan and Shang [18] demonstrated the use of different CZMs in FEM simulations of interfacial fracture of micrometer-thick films, showing that the cohesive strength and work of separation are the most dominant parameters in CZMs. Song and Komvopoulos [19] used a CZM that obeyed a bilinear traction-separation constitutive law to model the layer/substrate interface in an FEM analysis of adhesive contact between a rigid sphere and an elastic film attached to an elastic-perfectly plastic substrate and obtained numerical solutions that provided insight into the evolution of interfacial delamination during a full load-unload cycle. Mróz and Mróz [20] presented a CZM-based analytical study of progressive delamination in bilayer systems subjected to pure shear loading, which shed light on the mode of delamination, the effect of material properties on the damage process, the critical interface stress, and the fracture energy. Walter et al. [21] used different fracture mechanics methods to study the adhesive strength of a polyimide passivation layer on copper-film stacks deposited on a silicon substrate and the dependence of the critical energy release rate on the mode of loading and evaluated the delamination data using both analytical models and a CZM-FEM analysis.

More recently, Lin et al. [22] used a combined approach based on molecular dynamics (MD) simulations and a CZM-FEM analysis to study the interfacial fracture energy and delamination in multilayered integrated circuit packaging. Specifically, critical material parameters, such as the interfacial fracture energy, used in the interfacial cohesive constitutive law were derived from the MD simulations and were then input in the FEM model to analyze interfacial delamination in the multilayered structure due to indentation loading. Soroush et al. [23] developed an FEM model of interlaminar and intralaminar delamination damage in laminated composite plates subjected to impact using a CZM and a progressive damage model. Hassan et al. [24] introduced the interfacial strength and fracture toughness of a steel-steel bilayer sheet measured from a peel-off test into a CZM-FEM model to study interfacial delamination in the bilayer sheet caused by normal loading and provided experimental evidence showing more accurate estimates of delamination damage growth obtained with a liner-exponential traction-separation softening law than a linear softening law. Long et al. [25] used a CZM-FEM approach to investigate the failure characteristics of bimaterial systems in uniaxial tension and observed a transition from coating cracking to interface delamination with increasing coating thickness. Liang et al. [26] performed a CZM-FEM analysis of damage and fracture at the interfaces of ceramic films and metal substrates under uniaxial tensile loading and reported a dependence of the interfacial strength on both the residual radial force and the axial pressure and a catastrophic failure for thicker films.

Although the foregoing studies (and several others) greatly contributed to the elucidation of various challenging problems in interface mechanics, further research is needed to elucidate interface delamination in elastic-plastic homogeneous and layered media subjected to normal and shear (frictional) surface tractions. Consequently, the purpose of this study was to provide additional insight into interfacial delamination in half-spaces subjected to indentation and sliding contact loadings. To accomplish this objective, a CZM was incorporated in an FEM analysis to simulate interface separation when appropriate fracture energy conditions were satisfied. Simulation results revealing the evolution of subsurface stresses and plasticity illuminated the effects of indentation depth and sliding distance on interfacial delamination in homogeneous and layered half-spaces with different elastic-plastic properties, interfacial cohesive strength, and layer thickness. The present study elucidated the important role of elastic-plastic property mismatch at the layer/substrate interface of layered half-spaces and provided a modeling framework for analyzing interfacial delamination in multilayered structures subjected to quasistatic and dynamic contact loadings.

## 2 Modeling Approach

**2.1 Finite Element Model.** Figure 1 shows a schematic of the plane-strain contact problem of a rigid cylinder with a radius $R$ sliding against a deformable layered half-space examined in this study. After the cylinder indented the half-space up to a maximum depth $d$, it was slid laterally by a total distance $s$. The half-space consisting of a surface layer with a thickness $h = 0.1R$ and a half-space substrate was discretized by an $8R \times 8R$ FEM mesh having 36,162 four-node, reduced-integration, quadrilateral finite elements with a total of 37,658 nodes. The layer/substrate interface comprised pairs of nodes with initially the same coordinates. To accurately capture the large stress/strain gradients adjacent to the contact interface and the separation at the layer/substrate interface and to reduce the computational time, the mesh was compartmentalized into three segments centered at the point O of initial contact. The near-surface region of the mesh with dimensions $2h = 0.2R$ and $l = 2.2R$ was uniformly refined with elements having a size $l_c = 0.005R$, representing ~49% of the total number of elements, of which half were layer elements and the other half were substrate elements (inset of Fig. 1). Outside of this region, the substrate was meshed with elements with a size gradually increasing from $0.005R$ to $0.1R$. Finally, the outer part of the mesh was uniformly meshed with $0.1R$ size elements. The nodes at the bottom boundary of the mesh were constrained in both $x$- and $y$-directions, whereas the nodes at the left and right boundaries of the mesh were not constrained. All FEM simulations comprised three sequential phases, i.e., indentation of the half-space by the rigid cylinder to a depth $d$, sliding of the cylinder against the half-space in the $x$-direction by a distance $s$, and, finally, full unloading of the cylinder.

Surface contact was simulated with a finite sliding algorithm, which treated the surfaces of the deformable half-space and the rigid cylinder as slave and master surfaces, respectively, and controlled the relative separation and slip between the interacting surfaces. Each slave node coming into contact with the master surface was constrained to slide against the master surface, while the position of the slave node relative to the master surface was continuously tracked by the algorithm during the deformation. The finite sliding algorithm was implemented in the FEM analysis by using automatically generated contact elements. At each integration point of a contact element, the overclosure was adjusted to prevent a surface point of the deformed layer surface to penetrate the surface

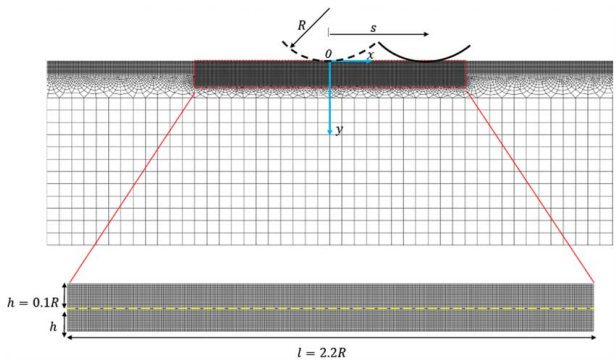


**Fig. 1 Finite element mesh (top) and refined mesh adjacent to the contact interface (bottom) (the dashed line corresponds to the delamination interface and the layer/substrate interface)**

of the rigid cylinder and the relative shear slip was computed afterward. Coulomb friction between the cylinder and the half-space surface was modeled by assigning to the contact elements a constant coefficient of friction equal to 0.1 that related the maximum allowable shear stress at the contact interface to the local contact pressure. All simulations were performed in displacement-control mode, using the multi-physics code ABAQUS/Standard (implicit solver) [27].

**2.2 Cohesive Zone Model and Interfacial Delamination.** Interfacial delamination under combined normal and tangential loading was modeled with a surface-based CZM for mixed-mode loading, depicted in Fig. 2. The CZM relates the effective cohesive interface traction $\bar{\sigma}$ to the effective separation $\bar{\delta}$ at the interface through the following linear relation [28]:

$$\bar{\sigma} = k\bar{\delta} = k\sqrt{\delta_n^2 + \delta_s^2} \tag{1}$$

where $k$ is the initial stiffness (a penalty parameter not representative of a physical quantity), and $\delta_n$ and $\delta_s$ are the relative separation distances in the normal and tangential directions, respectively. Ideally, the initial stiffness should be infinite so that not to affect the overall compliance of the model in the path OA (Fig. 2); however, a finite stiffness must be used to avoid numerical errors [27,29]. Preliminary simulations showed that $k = 10^6$ MPa/mm was a good choice for the present analysis; therefore, this stiffness value was used for both the normal and the tangential nodal displacements at the layer/substrate interface.

When the peak value of the applied traction was reached (point A in Fig. 2), the interfacial stiffness begun to degrade according to a damage initiation criterion. Various criteria for damage initiation have been proposed, such as the maximum nominal stress and quadratic nominal stress criteria. A comparative study [30] has shown a better agreement between experimental and FEM results based on the quadratic nominal stress criterion for damage initiation. According to this damage initiation criterion, interfacial delamination is instigated when the following traction-based relation is satisfied [28]:

$$\left(\frac{\langle t_n \rangle}{\sigma_c}\right)^2 + \left(\frac{t_s}{\tau_c}\right)^2 = 1 \tag{2}$$

where $t_n$ (= $k\delta_n$) and $t_s$ (= $k\delta_s$) are the interface tractions in the normal and tangential directions, and $\sigma_c$ and $\tau_c$ are the critical cohesive normal and tangential tractions, assumed equal to each other in this study. The Macaulay bracket (< >) used in Eq. (2) indicates that a purely compressive stress state does not initiate damage.

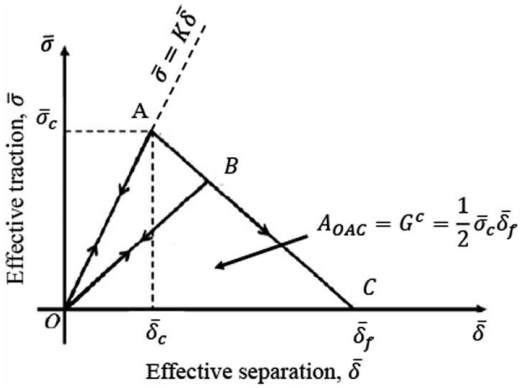


**Fig. 2 The cohesive model of the effective traction $\bar{\sigma}$ versus effective separation $\bar{\delta}$ at the delamination interface used in this study**

In mixed-mode loading, the critical separation distance $\bar{\delta}_c$ (point A in Fig. 2) at which Eq. (2) is satisfied is given by

$$\bar{\delta}_c = \left(\frac{\sigma_c}{k}\right)\left(\frac{\tau_c}{k}\right)\left[\frac{1+\gamma^2}{\left(\frac{\tau_c}{k}\right)^2 + \gamma^2\left(\frac{\sigma_c}{k}\right)^2}\right]^{1/2} \tag{3}$$

where $\gamma$ is the ratio of the shear displacement $\delta_s$ to the normal displacement $\delta_n$ of the node pairs, derived from Eq. (2) and the traction-displacement stiffness relations. Equations (2) and (3) were used to determine the initiation of delamination.

Stiffness degradation was represented by a linear softening behavior (path AC in Fig. 2) obeying the relation

$$\bar{\sigma} = \bar{\sigma}^*(1 - D) \tag{4}$$

where $\bar{\sigma}$ is the current effective interface cohesive strength, $\bar{\sigma}^*$ is the effective interface cohesive strength in the absence of damage, and $D$ is a scalar degradation parameter, given by

$$D = \frac{1 - \bar{\delta}_c/\bar{\delta}}{1 - \bar{\delta}_c/\bar{\delta}_f}, \quad 0 \le D \le 1 \tag{5}$$

where $\bar{\delta}_f$ is the effective separation distance corresponding to the fully degraded stiffness (point C in Fig. 2).

The area under the traction-separation response (OAC) is equal to the critical fracture energy $G^c$. For a substrate much thicker than the layer, the critical fracture energy in the normal and tangential interface directions $G_n^c$ and $G_s^c$, respectively, are given by [31,32]

$$G_n^c = \frac{1}{2}\left(\frac{h}{E'}\right)\sigma_c^2 \tag{6}$$

$$G_s^c = \frac{1}{2}\left(\frac{h}{G}\right)\tau_c^2 \tag{7}$$

where $h$ is the layer thickness, $E'$ is the effective elastic modulus, and $G$ is the shear modulus.

Under mixed-mode loading, the stiffness degradation and the parameter $\bar{\delta}_f$ depend on the following fracture energy-based criterion [28]:

$$\frac{G_n}{G_n^c} + \frac{G_s}{G_s^c} = 1 \tag{8}$$

where $G_n$ and $G_s$ are the fracture energies in the normal and shear (lateral) directions of the layer/substrate interface given by

$$G_n = \frac{k\bar{\delta}_c\bar{\delta}_f}{2(1+\gamma^2)} \tag{9}$$

$$G_s = \frac{k\bar{\delta}_c\bar{\delta}_f\gamma^2}{2(1+\gamma^2)} \tag{10}$$

Substitution of Eqs. (9) and (10) into Eq. (8) yields the following expression for $\bar{\delta}_f$:

$$\bar{\delta}_f = \frac{2(1+\gamma^2)}{\left(\frac{1}{G_n^c} + \frac{\gamma^2}{G_s^c}\right)k\bar{\delta}_c} \tag{11}$$

Accordingly, Eq. (11) was used to determine failure due to delamination.

FEM simulations that use CZMs often encounter convergence difficulties at the instant of node separation at the delamination interface, known to evolve from an elastic snap-back instability commencing when the stress reaches the interface cohesive strength. This convergence problem can be avoided by introducing a small fictitious viscosity in the CZM used to characterize the delamination interface [33]. Consequently, a small viscous dissipation parameter equal to 0.001, which resulted in negligibly small energy dissipation, was introduced into the CZM to prevent

instabilities due to the separation of the nodes at the delamination interface.

**2.3 Constitutive Model.** To model quasi-static, isothermal, isotropic strain-hardening material behavior, the half-space was modeled to obey the following constitutive law:

$$\sigma = E\varepsilon \ (\sigma < Y), \quad \sigma = K\varepsilon^n \ (\sigma \geq Y) \tag{12}$$

where $\sigma$ is the true stress, $\varepsilon$ is the true strain, $E$ is the elastic modulus, $Y$ is the yield strength, $K$ is the strength coefficient, and $n$ is the strain-hardening exponent (assumed equal to 0.2 in this study).

Yielding was determined by the von Mises equivalent stress $\sigma_{eq}$ yield criterion, given by

$$\sigma_{eq} = \left(\frac{3}{2}S_{ij}S_{ij}\right)^{1/2} = Y \tag{13}$$

where $S_{ij}$ are components of the deviatoric stress tensor.

The development of plasticity was traced by the equivalent plastic strain $\varepsilon^{p}_{eq}$, calculated by

$$\varepsilon^{p}_{eq} = \int_{\Omega}\left(\frac{2}{3}d\varepsilon^{p}_{ij}d\varepsilon^{p}_{ij}\right)^{1/2} \tag{14}$$

where $\Omega$ is the strain path used to track the accumulation of plasticity and $d\varepsilon^{p}_{ij}$ are plastic strain increments.

**2.4 Dimensionless Parameters.** To obtain generalized solutions, both input and output parameters were normalized by appropriate quantities. Specifically, the dimensionless indentation depth $\bar{d}$, sliding distance $\bar{s}$, and layer thickness $\bar{h}$ were defined by $d/R$, $s/R$, and $h/R$, respectively. This normalization of the foregoing dimensional parameters is appropriate because the cylinder radius represents the relevant length scale of the problem. In fact, the ratio $d/R$ has been used to represent the global deformation in numerous contact mechanics studies. The delamination fraction $\alpha$ was defined as the number of the separated node pairs at the layer/substrate interface divided by the total number of interface node pairs. The delamination ratio $\beta$ was determined as $\alpha_l/\alpha_h$, where $\alpha_l$ and $\alpha_h$ are the delamination fractions of a layered half-space with different layer properties and a homogeneous half-space with substrate properties, respectively. The elastic modulus ratio was defined as the elastic modulus of the layer $E_l$ divided by that of the substrate $E_s$, i.e., $\bar{E} = E_l/E_s$. Similarly, the yield strength ratio was defined as the yield strength of the layer $Y_l$ divided by that of the substrate $Y_s$, i.e., $\bar{Y} = Y_l/Y_s$. Thus, the values of the dimensionless parameters $\bar{E}$ and $\bar{Y}$ were indicative of the mismatch between the layer and substrate mechanical properties.

## 3 Results and Discussion

Interfacial decohesion (delamination) in a homogeneous elastic-plastic half-space is discussed first to establish a reference for the effects of normalized parameters, such as the sliding distance $\bar{s}$ and the indentation depth $\bar{d}$, and the interface cohesive strength $\sigma_c$ on interfacial delamination in a layered elastic-plastic half-space with varying elastic-plastic properties and layer thickness.

**3.1 Delamination in Homogeneous Half-Spaces.** The dependence of the effective nodal separation $\bar{\delta}$ at the cohesive interface before and after unloading on the sliding distance $\bar{s}$ and indentation depth $\bar{d}$ for a homogeneous elastic-plastic half-space can be interpreted in light of the results displayed in Fig. 3. For a short sliding distance ($\bar{s} = 0.1$), interfacial delamination was confined within a short distance from the center of indentation ($x/w = 0$), with unloading inducing a slight increase in effective nodal separation (Fig. 3(*a*)). For a fixed indentation depth ($\bar{d} = 0.002$), a longer

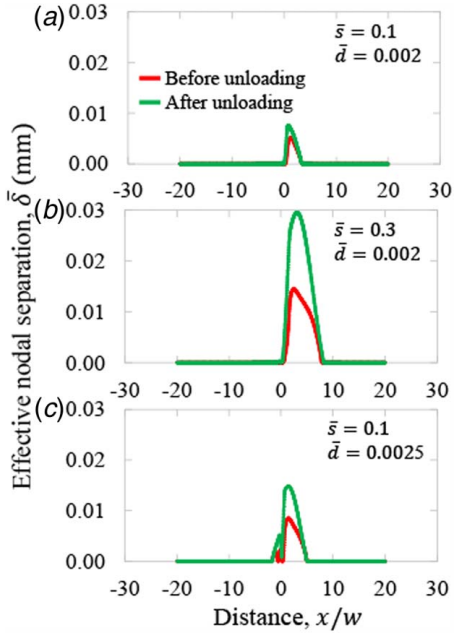


**Fig. 3 Effective nodal separation $\bar{\delta}$ profiles at the delamination interface ($\bar{h} = 1$) obtained (—) before and (—) after unloading versus distance $x/w$ measured from the center of initial contact ($x/w = 0$) for a homogeneous elastic-plastic half-space with $E$ = 100 GPa, $Y$ = 200 MPa, and $\sigma_c$ = 100 MPa: (*a*) $\bar{s} = 0.1$, $\bar{d} = 0.002$, (*b*) $\bar{s} = 0.3$, $\bar{d} = 0.002$, and (c) $\bar{s} = 0.1$, $\bar{d} = 0.0025$**

sliding distance ($\bar{s} = 0.3$) resulted in a profound increase in both the delamination length and the effective nodal separation, especially after unloading (Fig. 3(*b*)). Although the unloading did not affect the delamination length, it enhanced the effective nodal separation, particularly with the increase of the sliding distance. A similar trend was observed with the increase of the indentation depth ($\bar{d} = 0.0025$) (or load) for a fixed sliding distance ($\bar{s} = 0.1$) (Fig. 3(*c*)).

The dependence of the delamination fraction $\alpha$ on the sliding distance $\bar{s}$, cohesive strength $\sigma_c$, and indentation depth $\bar{d}$ is illustrated in Fig. 4. In all cases, the delamination fraction increased monotonically with the sliding distance. The simulations revealed two different tendencies. For a fixed indentation depth ($\bar{d} = 0.002$), a profound decrease of the delamination fraction occurred with increasing cohesive strength, because more energy was needed to separate the node pairs, whereas for a fixed cohesive strength ($\sigma_c = 100$ MPa), increasing the indentation depth from 0.002 to 0.0025 enhanced the delamination fraction significantly, especially with increasing sliding distance. For $\bar{s} = 0.3$ and $\sigma_c = 100$ MPa, for

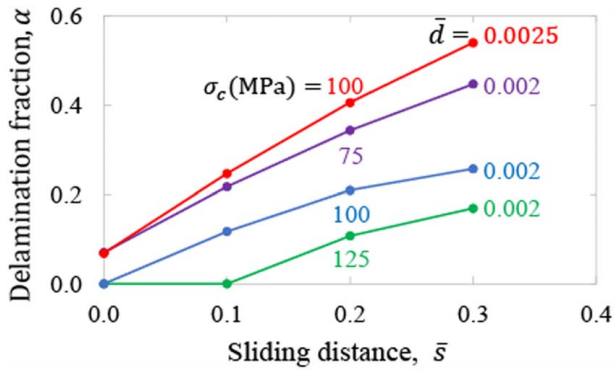


**Fig. 4 Delamination fraction $\alpha$ after unloading versus sliding distance $\bar{s}$ for a homogeneous elastic-plastic half-space with $E$ = 100 GPa, $Y$ = 200 MPa, $\bar{d} = 0.002$, 0.0025, and $\sigma_c$ = 75–125 MPa**

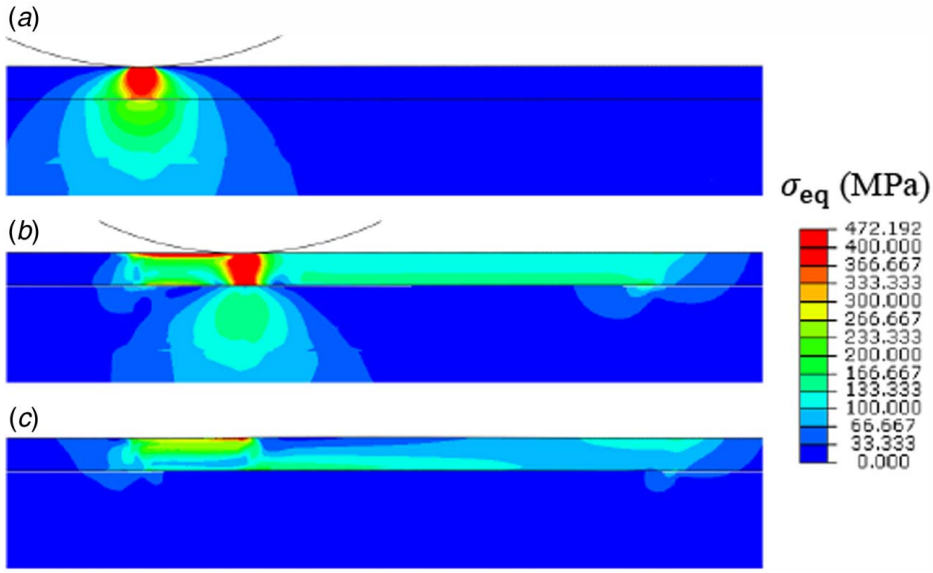


**Fig. 5 Contours of the equivalent von Mises stress $\sigma_{eq}$ for a homogeneous elastic-plastic half-space with $E = 100$ GPa, $Y = 200$ MPa, and $\sigma_c = 100$ MPa at three sequential simulation stages: (*a*) indentation ($\bar{d} = 0.002$), (*b*) sliding ($\bar{s} = 0.3$, $\bar{d} = 0.002$), and (c) unloading (the horizontal black line corresponds to the delamination interface)**

example, increasing the indentation depth by 25% fostered interfacial delamination more than twice. It is noted that for a relatively high cohesive strength and small indentation depth (or light load), pure indentation loading did not induce delamination.

The distributions of the equivalent von Mises stress $\sigma_{eq}$ in a homogeneous elastic-plastic half-space shown in Fig. 5 provided further insight into interfacial delamination due to indentation loading, sliding, and unloading. Because an indentation depth $\bar{d} = 0.002$ did not cause delamination for $\sigma_c = 100$ MPa (Fig. 4), the stress field was characteristic of an indented homogeneous half-space (Fig. 5(*a*)). However, sliding by a distance $\bar{s} = 0.3$ induced delamination at the cohesive interface (Figs. 3(*b*) and 4), resulting in localized stress discontinuities and stress intensification in the region above the partially delaminated cohesive interface (Fig. 5(*b*)). Unloading promoted the lateral expansion of the high residual stresses above the cohesive interface (Fig. 5(*c*)), attributed to the increase of the effective nodal separation in the delaminated portion of the cohesive interface upon unloading (Fig. 3(*b*)).

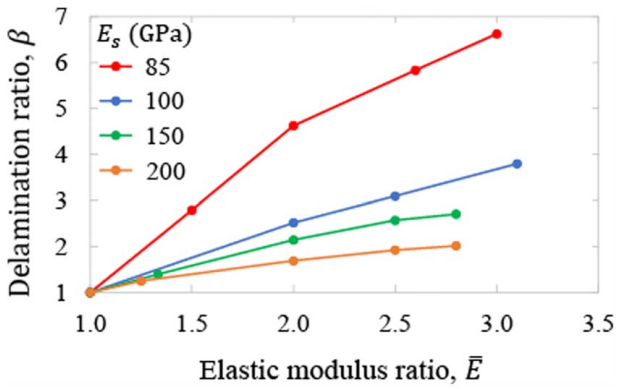


**Fig. 6 Delamination ratio $\beta$ after unloading versus elastic modulus ratio $\bar{E}$ for an elastic layered half-space with $E_s = 85$–200 GPa and $\sigma_c = 100$ MPa ($\bar{h} = 0.1$, $\bar{d} = 0.002$, and $\bar{s} = 0.1$)**

**3.2 Delamination in Layered Half-Spaces.** Simulation results for layered elastic half-spaces are presented first to illuminate the effect of the elastic modulus mismatch (represented by the elastic modulus ratio $\bar{E}$) on the delamination at the layer/substrate interface, hereafter referred to as interfacial delamination. Figure 6 shows the variation of the delamination ratio $\beta$ after unloading with the elastic modulus ratio $\bar{E}$ for $E_s = 85$–200 GPa. The figure reveals two important trends. First, all simulation cases demonstrated a monotonic increase in $\beta$ with $\bar{E}$, originating from a common point ($\beta = 1$) corresponding to the homogeneous half-space case ($\bar{E} = 1$). The tendency for interfacial delamination to intensify with increasing elastic modulus mismatch can be attributed to the proliferation of the interfacial stresses due to layer stiffening, leading to further nodal separation upon unloading. Second, a nonlinear increase in $\beta$ with decreasing $E_s$ occurred for fixed $E_l$. This trend does not imply that a more compliant substrate promotes delamination; rather it suggests a more prominent effect of the layer's elastic modulus on interfacial delamination for more compliant substrates. For $\bar{E} = 2.5$, for instance, the delamination length was about 5.5 and 2 times greater than that corresponding to a homogeneous elastic half-space with $E_s = 85$ and 200 GPa, respectively.

The foregoing result can be explained by considering the stresses produced by the sliding process in elastic layered half-spaces with different layer and substrate elastic moduli. Figure 7 shows contours of the equivalent von Mises stress $\sigma_{eq}$ in an elastic layered half-space produced before unloading for various $\bar{E}$ values and the corresponding delamination fraction $\alpha$. For a fixed substrate elastic modulus ($E_s = 100$ GPa), layer stiffening intensified the stresses in the layer and the layer/substrate interface, consequently increasing the delamination fraction (Figs. 7(*a*)–7(*c*)). In the case of a homogeneous half-space ($\bar{E} = 1$), high stresses developed below the contact interface and interfacial delamination was limited ($\alpha = 0.05$) due to minor stress intensification at the delamination interface (Fig. 7(*a*)). The tensile and shear stresses arising at the interface nodal points slightly to the right of the cylinder increased the effective nodal separation locally, causing delamination at those node pairs where the decohesion condition (Eq. (2)) was satisfied. The increase in layer stiffness, significantly fortified the stresses at the layer/substrate interface, consequently increasing the delamination fraction by a factor of about 3 and 4, i.e., $\alpha = 0.13$ and 0.20 for

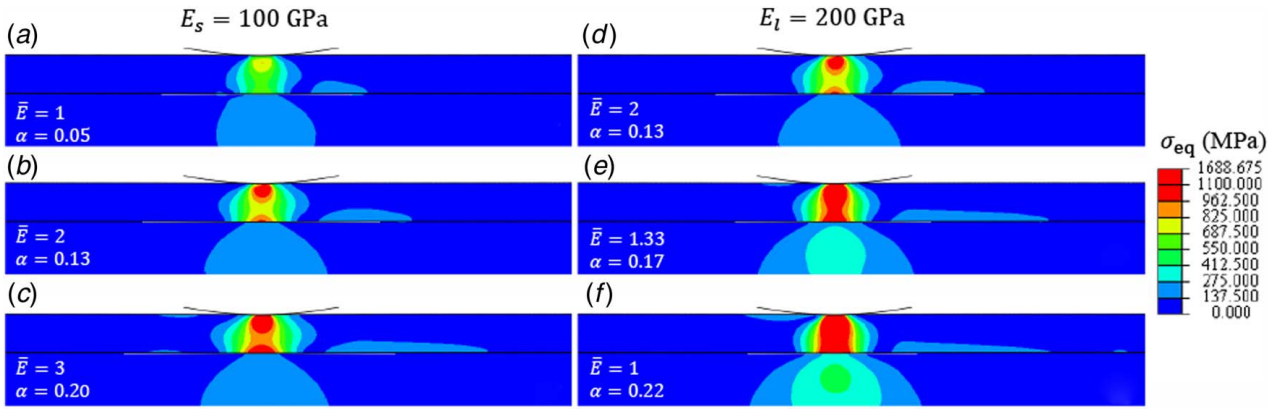


**Fig. 7 Contours of the equivalent von Mises stress $\sigma_{eq}$ versus elastic modulus ratio $\bar{E}$ and delamination fraction $\alpha$ obtained before unloading for an elastic layered half-space with (*a*)–(*c*) $E_s = 100$ GPa and $E_l = 100$, 200, and 300 GPa ($\bar{E} = 1$, 2, and 3, respectively), (*d*)–(*f*) $E_l = 200$ GPa and $E_s = 100$, 150, and 200 GPa ($\bar{E} = 2$, 1.33, and 1, respectively), and $\sigma_c = 100$ MPa ($h = 0.1$, $d = 0.002$, and $s = 0.1$) (the horizontal black line corresponds to the delamination interface)**

$\bar{E} = 2$ and 3, respectively (Figs. 7(*b*) and 7(*c*)). A similar trend was observed with the decrease of the substrate stiffness, characterized by the augmentation of interfacial delamination. Specifically, for the most compliant substrate ($\bar{E} = 2$), high stresses developed below the contact interface and across a small interfacial region, resulting in localized delamination ($\alpha = 0.13$) (Fig. 7(*d*)). Substrate stiffening promoted the evolution of much higher stresses in the layer and the layer/substrate interface, contributing to an increase in delamination fraction with substrate stiffness, i.e., $\alpha = 0.17$ and 0.22 for $\bar{E} = 1.33$ and 1, respectively (Figs. 7(*e*) and 7(*f*)).

Simulation results for elastic-plastic layered media are presented next to reveal the effect of plasticity on the evolution of interfacial delamination. Figure 8 shows the delamination fraction $\alpha$ after unloading versus the yield strength ratio $\bar{Y}$. Although interfacial delamination did not occur for $Y_s = 50$ MPa, all other simulations demonstrated an initial increase in $\alpha$ with $\bar{Y}$ followed by a decrease beyond a certain $\bar{Y}$ value, depending on the yield strength of the substrate $Y_s$. Specifically, the maximum $\alpha$ for $Y_s = 100$, 200, and 300 MPa corresponded to $\bar{Y} \cong 1.3$, 0.75, and 0.5, respectively. Moreover, although a higher yield strength of the substrate produced a higher delamination fraction in the low range of $\bar{Y}$, an opposite tendency occurred in the high range of $\bar{Y}$, where the delamination fraction decreased sharply. This trend is also reflected in the results of the effective nodal separation presented next.

Figure 9 shows distributions of the effective nodal separation $\bar{\delta}$ before and after unloading for a layered elastic-plastic half-space with $\bar{Y} = 0.75$ and 1. Before unloading, significantly larger nodal separation distances were encountered with the relatively lower strength layer ($\bar{Y} = 0.75$), especially in the region $-10 < x/w < 0$, compared to the higher strength layer ($\bar{Y} = 1.5$). A notable amplification of the nodal separation distances originated upon unloading, especially for $\bar{Y} = 0.75$, where much larger nodal separations developed in the interfacial region $0 < x/w < 12$ and much lower in the region $-10 < x/w < 0$, contrary to what was found before unloading. This can be attributed to the effect of residual stresses in the layer causing it to conform and the nodal separations to adjust accordingly. For $\bar{Y} = 1.5$, however, the increase in nodal separation upon unloading was much less pronounced than that for $\bar{Y} = 0.75$. The difference between these two cases can also be quantified in terms of the delamination fraction, i.e., $\alpha = 0.55$ and 0.62 ($\bar{Y} = 0.75$) and $\alpha = 0.27$ and 0.27 ($\bar{Y} = 1.5$) before and after unloading, respectively. Despite the increase of the effective nodal separation in Fig. 9(*b*), the delamination fraction did not change upon unloading because the delamination criteria (Eqs. (2)–(11)) were

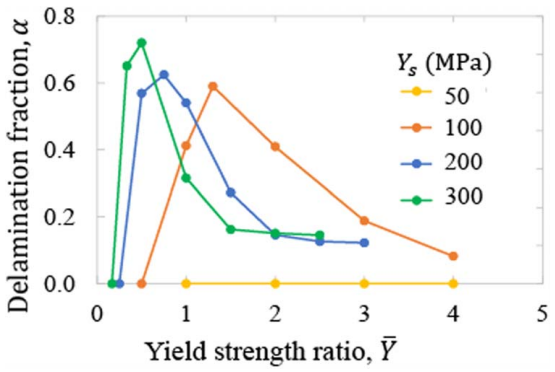


**Fig. 8 Delamination fraction $\alpha$ after unloading versus yield strength ratio $\bar{Y}$ for an elastic-plastic layered half-space with $E_l = E_s = 100$ GPa ($\bar{E} = 1$), $Y_s = 50$–300 MPa, and $\sigma_c = 100$ MPa ($h = 0.1$, $d = 0.0025$, and $s = 0.3$)**

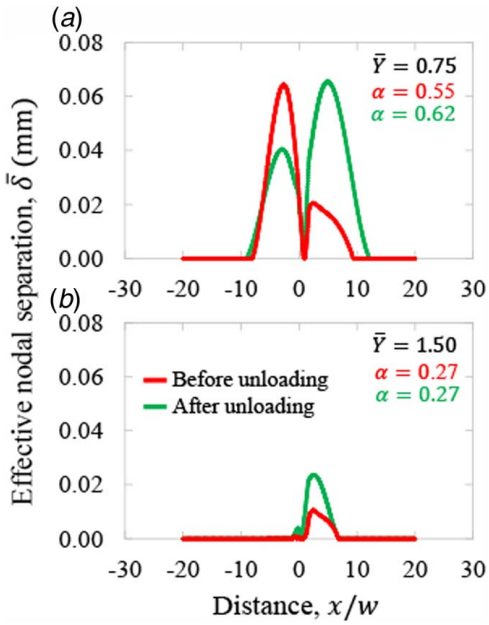


**Fig. 9 Effective nodal separation $\bar{\delta}$ profiles at the delamination interface ($\bar{h} = 1$) obtained (—) before and (—) after unloading versus distance $x/w$ measured from the center of initial contact ($x/w = 0$) for a layered elastic-plastic half-space with $E_l = E_s = 100$ GPa ($\bar{E} = 1$), $E_s = 200$ MPa, (*a*) $Y_l = 150$ MPa ($\bar{Y} = 0.75$), (*b*) $Y_l = 300$ MPa ($\bar{Y} = 1.5$), and $\sigma_c = 100$ MPa ($\bar{h} = 0.1$, $\bar{d} = 0.0025$, and $\bar{s} = 0.3$)**

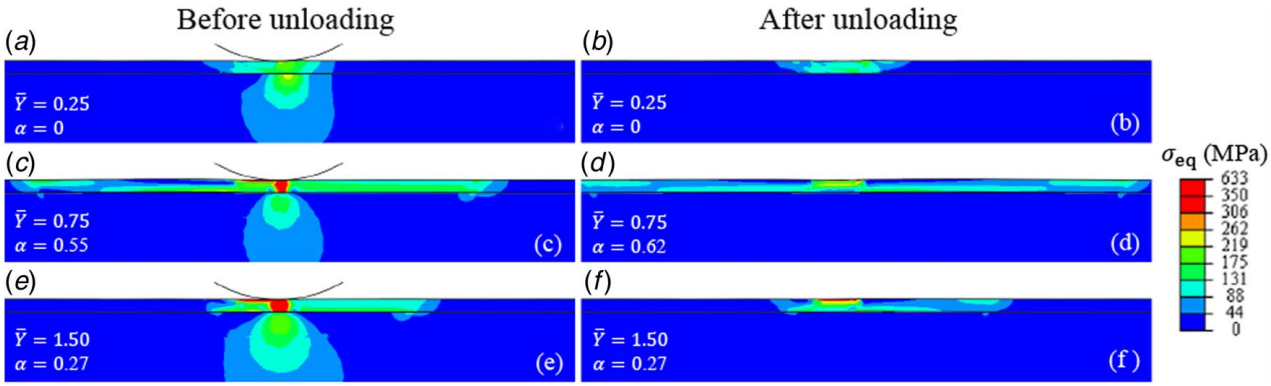


**Fig. 10 Contours of the equivalent von Mises stress $\sigma_{eq}$ before (left) and after (right) unloading versus yield strength ratio $\bar{Y}$ and delamination fraction $\alpha$ for an elastic-plastic layered half-space with $E_l = E_s = 100$ GPa ($\bar{E} = 1$), $Y_s = 200$ MPa, $Y_l = 50$, 150, and 300 MPa ($\bar{Y} = 0.25$, 0.75, and 1.5, respectively), and $\sigma_c = 100$ MPa ($\bar{h} = 0.1$, $\bar{d} = 0.0025$, and $\bar{s} = 0.3$) (the horizontal black line corresponds to the delamination interface)**

not satisfied in this case. This was also the reason for the constancy of the delamination fraction seen in some of the unloading simulations presented in the following figures. The results shown in Fig. 9 illustrate that increasing $\bar{Y}$ (or $Y_l$) by a factor of 2 decreased $\bar{\delta}_{max}$ by a factor of ~3 and the delamination length by a factor >2, indicating a profound effect of the yield strength of the layer on interfacial delamination.

The results shown in Figs. 8 and 9 can be interpreted by considering the effect of the yield strength ratio $\bar{Y}$ on the subsurface stress and strain fields before and after unloading. Figure 10 shows contours of the von Mises equivalent stress $\sigma_{eq}$ in an elastic-plastic layered half-space for different values of the yield strength ratio $\bar{Y}$. For $\bar{Y} = 0.25$ (Fig. 10(*a*)), two small pockets of high stress formed before unloading, one adjacent to the contact interface and another in the substrate just below the layer/substrate interface. However, the generated interfacial stresses did not satisfy the fracture energy criteria to instigate delamination ($\alpha = 0$), consistent with the result shown in Fig. 8. For $\bar{Y} = 0.75$ (Fig. 10(*c*)), significantly higher stresses occurred in the layer, spreading laterally and through the layer/substrate interface and causing interfacial delamination ($\alpha = 0.55$). For $\bar{Y} = 1.5$ (Fig. 10(*e*)), a larger zone of high stresses developed in the layer; nonetheless, both stress spreading within the layer and delamination were less ($\alpha = 0.27$) than those for $\bar{Y} = 0.75$. All simulations demonstrated extremely small residual stresses in the substrate just below the layer/substrate interface after unloading, suggesting that plastic deformation was confined within the layer and at the layer/substrate interface. A comparison of Figs. 10(*b*), 10(*d*), and 10(*f*) indicates that, although the increase in $\bar{Y}$ progressively intensified the residual stresses, the effect on the delamination length did not show a specific trend. Specifically, for $\bar{Y} = 0.75$ (Fig. 10(*d*)), the delamination length increased from 0.55 to 0.62 after unloading, whereas for $\bar{Y} = 1.5$ (Fig. 10(*f*)), the effect of unloading on the delamination length was negligible.

The contours of the equivalent plastic strain $\varepsilon^p_{eq}$ shown in Fig. 11 provided further insight into the previous findings, confirming the strong effect of the yield strength of the layer on interfacial delamination. Despite widespread plastic deformation in the bulk of the layer and at the layer/substrate interface for $\bar{Y} = 0.25$ (Fig. 11(*a*)), the relatively low stresses in the low-strength layer (Fig. 10(*a*)) did not lead to delamination ($\alpha = 0$). Moreover, while layer strengthening ($\bar{Y} = 0.75$) reduced widespread plasticity in the layer (Fig. 11(*b*)), it also intensified the stresses at the layer/substrate interface (Fig. 10(*c*)), resulting in delamination ($\alpha = 0.55$), which was further augmented upon unloading ($\alpha = 0.62$) (Fig. 11(*b*)). Interestingly, further layer strengthening ($\bar{Y} = 1.5$) reduced plasticity in the layer significantly, with large plastic strains confined into the upper region of the layer (Fig. 11(*c*)); but, although this was accompanied by stress intensification (Fig. 10(*e*)), delamination decreased and remained unaffected even after unloading ($\alpha = 0.27$) (Fig. 10(*f*)). A similar result was encountered by varying the yield strength of the substrate, while maintaining a high yield strength of the layer (Figs. 11(*d*)–11(*f*)),

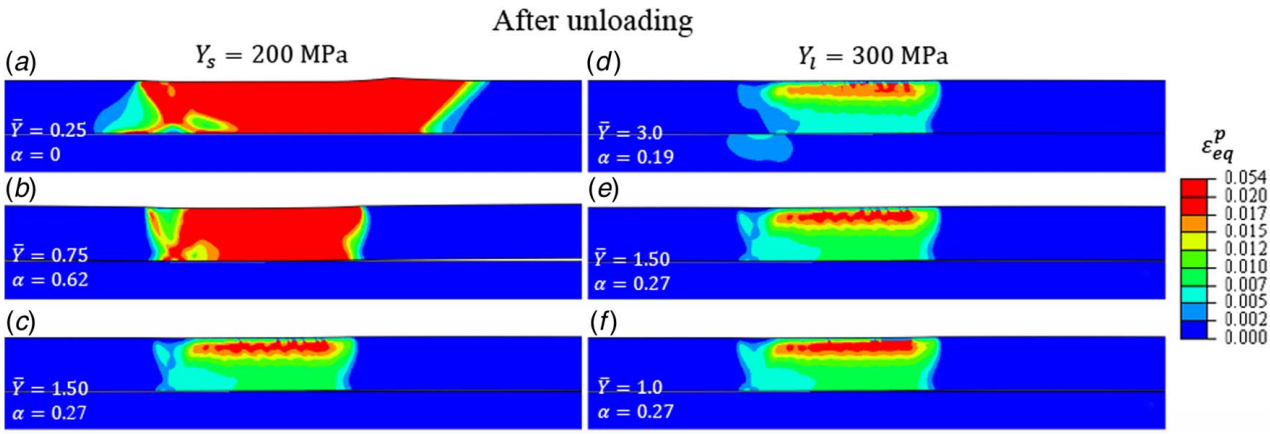


**Fig. 11 Contours of the equivalent plastic strain $\varepsilon^p_{eq}$ after unloading versus yield strength ratio $\bar{Y}$ and delamination fraction $\alpha$ for an elastic-plastic layered half-space with $E_l = E_s = 100$ GPa ($\bar{E} = 1$), (*a*)–(*c*) $Y_s = 200$ MPa and $Y_l = 50$, 150, and 300 MPa ($\bar{Y} = 0.25$, 0.75, and 1.5, respectively), (*d*)–(*f*) $Y_l = 300$ MPa and $Y_s = 100$, 200, and 300 MPa ($\bar{Y} = 3$, 1.5, and 1, respectively), and $\sigma_c = 100$ MPa ($\bar{h} = 0.1$, $\bar{d} = 0.0025$, and $\bar{s} = 0.3$) (the horizontal black line corresponds to the delamination interface)**

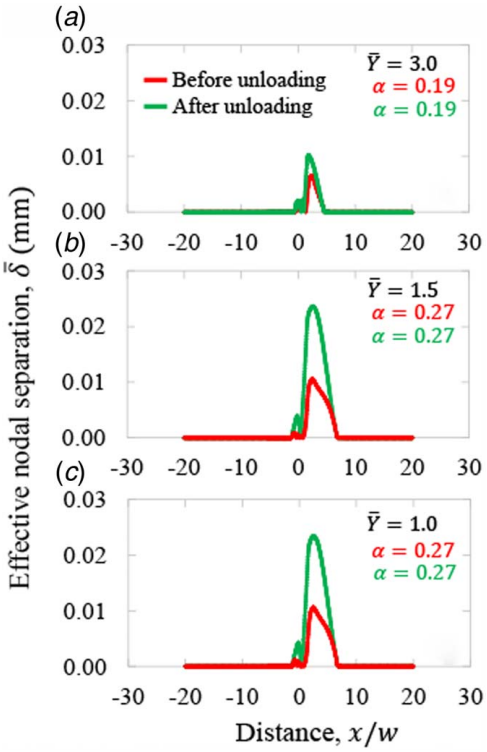


**Fig. 12 Effective nodal separation $\bar{\delta}$ profiles at the delamination interface ($\bar{h} = 1$) obtained (—) before and (—) after unloading versus distance $x/w$ measured from the center of initial contact ($x/w = 0$) for a layered elastic-plastic half-space with $E_l = E_s =$ 100 GPa ($\bar{E} = 1$), $Y_l = 300$ MPa, (*a*) $Y_s = 100$ MPa ($\bar{Y} = 3$), (*b*) $Y_s =$ 200 MPa ($\bar{Y} = 1.5$), (c) $Y_s = 300$ MPa ($\bar{Y} = 1$), and $\sigma_c = 100$ MPa ($\bar{h} = 0.1$, $\bar{d} = 0.0025$, and $\bar{s} = 0.3$)**

signifying a dominant effect of layer plasticity on interfacial delamination.

Figure 12 shows distributions of the effective nodal separation $\bar{\delta}$ acquired before and after unloading of an elastic-plastic layered half-space for different values of the yield strength ratio $\bar{Y}$. These results provided additional supporting proof to the foregoing contention. In all simulation cases, unloading enhanced surface separation without affecting the delamination fraction. The highest yield strength ratio ($\bar{Y} = 3$) produced the smallest nodal surface separations and delamination fraction ($\alpha = 0.19$) (Fig. 12(*a*)). Decreasing $\bar{Y}$ instigated larger delamination gaps, but only a small increase in delamination fraction, i.e., $\alpha = 0.27$ for both $\bar{Y} = 1.5$ (Fig. 12(*b*)) and $\bar{Y} = 1$ (Fig. 12(*c*)). The results shown in Fig. 12 can be further interpreted by examining the corresponding stress fields before and after unloading, shown in Fig. 13. A comparison of the stress fields before or after unloading shows close similarity, despite less stress spreading in the layer for $\bar{Y} = 3$ than $\bar{Y} = 1.5$ and 1, consistent with the corresponding delamination fractions and the variation of $\alpha$ with $\bar{Y}$ displayed in Fig. 8.

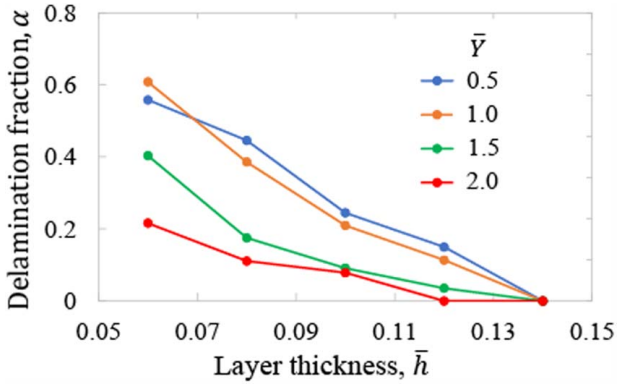


**Fig. 14 Delamination fraction $\alpha$ after unloading versus delamination layer thickness $\bar{h}$ for an elastic-plastic layered half-space with $E_l = E_s = 100$ GPa ($\bar{E} = 1$), $Y_s = 200$ MPa, $Y_l = 100$–$400$ MPa ($\bar{Y} = 0.5$–$2$, respectively) and $\sigma_c = 100$ MPa ($\bar{d} = 0.002$, $\bar{s} = 0.2$)**

In addition to the elastic-plastic material properties of the layered half-space, the layer thickness is another important parameter affecting the stresses arising at the layer/substrate interface and, consequently, interfacial delamination. Figure 14 shows the delamination fraction $\alpha$ after unloading as a function of layer thickness $\bar{h}$ for different values of $\bar{Y}$. All simulation cases displayed a monotonic decrease in $\alpha$ with increasing $\bar{h}$ and $\bar{Y}$. This trend can be explained by considering that a thicker and stronger layer can accommodate much higher stresses compared to a thinner and weaker layer, hence significantly lessening the stresses at the layer/substrate interface and in the bulk of the substrate. In fact, the material near the interface may not even experience plastic deformation in the case of a thicker layer, despite the material property mismatch between the layer and the substrate.

## 4 Conclusions

A contact mechanics analysis of interfacial delamination in homogeneous and layered elastic and elastic-plastic half-spaces subjected to normal and shear tractions generated by indentation

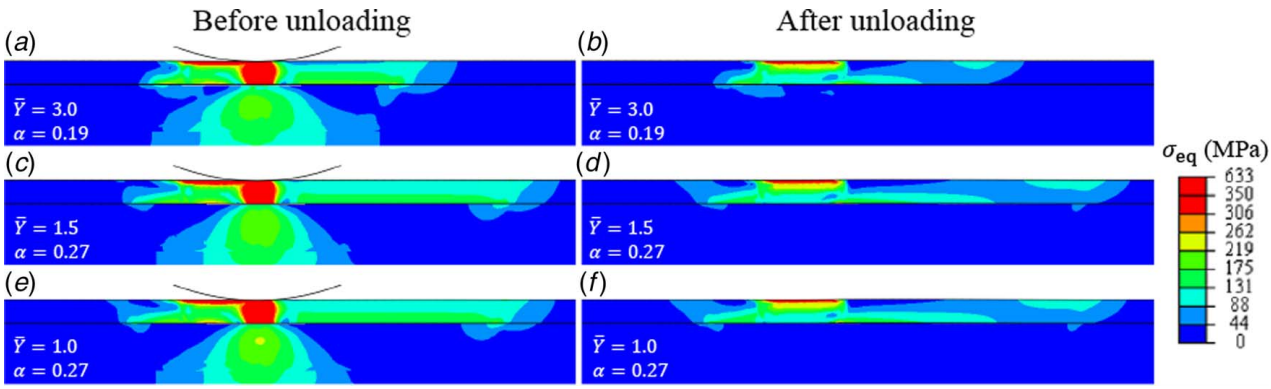


**Fig. 13 Contours of the equivalent von Mises stress $\sigma_{eq}$ before (left) and after (right) unloading versus yield strength ratio $\bar{Y}$ and delamination fraction $\alpha$ for an elastic-plastic layered half-space with $E_l = E_s = 100$ GPa ($\bar{E} = 1$), $Y_s = 300$ MPa, $Y_s = 100$, 200, and 300 MPa ($\bar{Y} = 3$, 1.5, and 1, respectively), and $\sigma_c = 100$ MPa ($\bar{h} = 0.1$, $\bar{d} = 0.0025$, and $\bar{s} = 0.3$) (the horizontal black line corresponds to the delamination interface)**

and sliding was performed in this study. A surface-based CZM was implemented in an FEM analysis to model nodal separation at the delamination interface (layer/substrate interface for layered half-spaces) when appropriate fracture energy conditions were satisfied. A parametric study demonstrated that increasing the indentation depth and/or sliding distance and decreasing the cohesive strength enhanced interfacial delamination in homogeneous elastic-plastic half-spaces, even more after unloading, the primary reason being the high stresses spreading in the region above the delamination interface. An elastic FEM analysis of layered half-spaces showed that increasing the elastic modulus of the layer while fixing that of the substrate resulted in high stress localization, whereas the reverse caused more pronounced stress intensification in the bulk of the layer and its interface with the substrate, with both scenarios leading to the enhancement of delamination at the layer/substrate interface. Simulations of an elastic-plastic FEM analysis demonstrated a significant effect of the yield strength mismatch between the layer and the substrate on the delamination process, characterized by a transition from increasing to decreasing delamination with the increase of the layer-to-substrate yield strength ratio. This trend was attributed to a change from intensifying to lessening subsurface stresses and less plastic deformation in the layer and the layer/substrate interface. The effect of layer strengthening on interfacial delamination was more profound than that of substrate stiffening. Moreover, increasing the layer thickness while maintaining a high yield strength of the layer effectively suppressed delamination at the layer/substrate interface. The results of this study provided insight into the effects of indentation depth, sliding distance, and elastic-plastic property mismatch between the layer and substrate of layered half-spaces on interfacial delamination. The present analysis can be further extended to include a plasticity-induced damage model for studying cumulative damage in strain-hardening half-spaces subjected to cyclic dynamic contact loading by a rigid surface exhibiting multiscale roughness.

## Conflict of Interest

There are no conflicts of interest.

## Data Availability Statement

The authors attest that all data for this study are included in the paper.

## References


[1] Kim, J.-H., Kil, H.-J., Lee, S., Park, J., and Park, J.-W., 2022, "Interfacial Delamination at Multilayer Thin Films in Semiconductor Devices," ACS Omega, **7**(29), pp. 25219–25228.

[2] Morris, B. A., 2022, *The Science and Technology of Flexible Packaging: Multilayer Films From Resin and Process to End Use*, 2nd ed., Elsevier, Amsterdam, The Netherlands.

[3] Ügdüler, S., De Somer, T., Van Geem, K. M., Roosen, M., Kulawig, A., Leineweber, R., and De Meester, S., 2021, "Towards a Better Understanding of Delamination of Multilayer Flexible Packaging Films by Carboxylic Acids," ChemSusChem, **14**(19), pp. 4198–4213.

[4] Ko, S. W., Dechakupt, T., Randall, C. A., Trolier-McKinstry, S., Randall, M., and Tajuddin, A., 2010, "Chemical Solution Deposition of Copper Thin Films and Integration Into a Multilayer Capacitor Structure," J. Electroceram., **24**(3), pp. 161–169.

[5] Suh, N. P., 1973, "The Delamination Theory of Wear," Wear, **25**(1), pp. 111–124.

[6] Voevodin, A. A., Schneider, J. M., Rebholz, C., and Matthews, A., 1996, "Multilayer Composite Ceramicmetal-DLC Coatings for Sliding Wear Applications," Tribol. Int., **29**(7), pp. 559–570.

[7] Cho, S.-S., and Komvopoulos, K., 1997, "Wear Mechanisms of Multi-Layer Coated Cemented Carbide Cutting Tools," ASME J. Tribol., **119**(1), pp. 8–17.

[8] Tabakov, V. P., Vereschaka, A. S., and Vereschaka, A. A., 2017, "Multilayer Composition Coatings for Cutting Tools: Formation and Performance Properties," Mech. Ind., **18**(7), p. 706.

[9] Choi, S. R., Hutchinson, J. W., and Evans, A. G., 1999, "Delamination of Multilayer Thermal Barrier Coatings," Mech. Mater., **31**(7), pp. 431–447.

[10] Murthy, A. K., Komvopoulos, K., and Brown, S. D., 1990, "Processing and Characterization of Multi-Layered Wear-Resistant Ceramic Coatings," ASME J. Eng. Mater. Technol., **112**(2), pp. 164–174.

[11] Nagarathnam, K., and Komvopoulos, K., 1993, "Microstructural Characterization and *In Situ* Transmission Electron Microscopy Analysis of Laser-Processed and Thermally Treated Fe-Cr-W-C Clad Coatings," Metal. Trans. A, **24**(7), pp. 1621–1629.

[12] Gerberich, W. W., Kramer, D. E., Tymiak, N. I., Volinsky, A. A., Bahr, D. F., and Kriese, M. D., 1999, "Nanoindentation-Induced Defect–Interface Interactions: Phenomena, Methods and Limitations," Acta Mater., **47**(15–16), pp. 4115–4123.

[13] He, M. Y., Hutchinson, J. W., and Evans, A. G., 2011, "A Stretch/Bend Method for In Situ Measurement of the Delamination Toughness of Coatings and Films Attached to Substrates," ASME J. Appl. Mech., **78**(1), p. 011009.

[14] Liu, M., and Yang, F., 2012, "Finite Element Analysis of the Indentation-Induced Delamination of Bi-Layer Structures," J. Comput. Theoret. Nanosci., **9**(6), pp. 851–858.

[15] Dugdale, D. S., 1960, "Yielding of Steel Sheets Containing Slits," J. Mech. Phys. Solids, **8**(2), pp. 100–104.

[16] Barenblatt, G. I., 1962, "The Mathematical Theory of Equilibrium Cracks in Brittle Fracture," Adv. Appl. Mech., **7**, pp. 55–129.

[17] Alfano, M., Furgiuele, F., Leonardi, A., Maletta, C., and Paulino, G. H., 2009, "Mode I Fracture of Adhesive Joints Using Tailored Cohesive Zone Models," Int. J. Fract., **157**(1–2), pp. 193–204.

[18] Yan, Y., and Shang, F., 2009, "Cohesive Zone Modeling of Interfacial Delamination in PZT Thin Films," Int. J. Solids Struct., **46**(13), pp. 2739–2749.

[19] Song, Z., and Komvopoulos, K., 2013, "Delamination of an Elastic Film From an Elastic–Plastic Substrate During Adhesive Contact Loading and Unloading," Int. J. Solids Struct., **50**(16–17), pp. 2549–2560.

[20] Mróz, Z., and Mróz, K. P., 2015, "Analysis of Delamination and Damage Growth in Joined Bi-Layer Systems," Geomech. Energy Environ., **4**, pp. 4–28.

[21] Walter, T., Lederer, M., and Khatibi, G., 2016, "Delamination of Polyimide/Cu Films Under Mixed Mode Loading," Microelect. Relat., **64**, pp. 281–286.

[22] Lin, P., Shen, F., Yeo, A., Liu, B., Xue, M., Xu, H., and Zhou, K., 2017, "Characterization of Interfacial Delamination in Multi-Layered Integrated Circuit Packaging," Surf. Coat. Technol., **320**, pp. 349–356.

[23] Soroush, M., Malekzadeh Fard, K., and Shahravi, M., 2018, "Finite Element Simulation of Interlaminar and Intralaminar Damage in Laminated Composite Plates Subjected to Impact," Lat. Am. J. Solids Struct., **15**(6), p. e90.

[24] Hassan, M., Ali, A., Ilyas, M., Hussain, G., and ul Haq, I., 2019, "Experimental and Numerical Simulation of Steel/Steel (St/St) Interface in Bi-Layer Sheet Metal," Int. J. Lightweight Mater. Manuf., **2**(2), pp. 89–96.

[25] Long, H., Liang, L., and Wei, Y., 2019, "Failure Characterization of Solid Structures Based on an Equivalence of Cohesive Zone Model," Int. J. Solids Struct., **163**, pp. 194–210.

[26] Liang, L., Chen, L., Wu, L., and Tan, H., 2021, "Interface Strength, Damage and Fracture Between Ceramic Films and Metallic Substrates," Materials, **14**(2), p. 353.

[27] ABAQUS Analysis User's Guide, 2022.

[28] Camanho, P. P., Davila, C. G., and de Moura, M. F., 2003, "Numerical Simulation of Mixed-Mode Progressive Delamination in Composite Materials," J. Compos. Mater., **37**(16), pp. 1415–1438.

[29] Turon, A., Dávila, C. G., Camanho, P. P., and Costa, J., 2007, "An Engineering Solution for Mesh Size Effects in the Simulation of Delamination Using Cohesive Zone Models," Eng. Fract. Mech., **74**(10), pp. 1665–1682.

[30] Rocha, R. J. B., and Campilho, R. D. S. G., 2018, "Evaluation of Different Modelling Conditions in the Cohesive Zone Analysis of Single-Lap Bonded Joints," J. Adhes., **94**(7), pp. 562–582.

[31] Krenk, S., 1992, "Energy Release Rate of Symmetric Adhesive Joints," Eng. Fract. Mech., **43**(4), pp. 549–559.

[32] Freund, L., and Suresh, S., 2004, *Thin Film Materials: Stress, Defect Formation and Surface Evolution*, Cambridge University Press, Cambridge, UK.

[33] Gao, Y. F., and Bower, A. F., 2004, "A Simple Technique for Avoiding Convergence Problems in Finite Element Simulations of Crack Nucleation and Growth on Cohesive Interfaces," Model. Simul. Mater. Sci. Eng., **12**(3), pp. 453–463.